# Application of Iterative Moment-Method Solutions to Ocean Surface Radar Scattering

D. J. Donohue, H.-C. Ku, and Donald R. Thompson

***Abstract*— Numerical methods such as the banded matrix iterative approach (BMIA) represent a major advance in the direct numerical simulation of rough surface-wave scattering. This paper considers the application of iterative methods such as the BMIA to ocean-radar scattering. It is shown that for typical microwave radar frequencies and sea-surface roughness, the BMIA is actually of limited use. A more general iterative solution based on a multigrid decomposition and the generalized conjugate residual (GCR) method, is thus developed. The multigrid approach is ideally suited to the broad-band ocean surface, as it solves the scattering problem on a sequence of grids, each corresponding to a different range of spatial frequencies or length scales. This approach is applied here to several sea scattering problems, including very low grazing angles and both horizontal and vertical polarization. Good agreement is obtained with perturbation theory in the appropriate limits and several qualitative characteristics of radar backscatter data are reproduced.**

***Index Terms*—Sea surface electromagnetic scattering.**

## I. Introduction

THE need for numerical methods in the study of low-grazing-angle scatter from rough surfaces is now well established. Effects such as multiple scattering, shadowing, and diffraction, which are difficult to model in theory, become increasingly important in the grazing limit. Unfortunately, even numerical methods encounter difficulties in this limit. In many cases, the numerical method either breaks down or the application becomes computationally intensive to the point of being impractical.

Direct numerical simulation of the scattering problem via the method of moments is apparently one of the few sufficiently accurate methods for low-grazing-angle scatter. This paper considers the application of moment methods to ocean surface radar scatter. Given the typical range of radar wavelengths, illumination footprint size, and ocean surface length scales, this problem usually requires a large number of unknowns ($N$), perhaps numbering in the tens of thousands for two-dimensional (2-D) models. Problems of this size can often be impractical, even on the current generation of high-performance workstations. Given that the usual approach to the random ocean surface problem is a Monte Carlo method in which scattering statistics are generated over a large number of surface realizations and that one is typically interested in a range of parameters such as wind speed and incidence angle, the computational challenge is even more apparent.

Manuscript received April 21, 1997; revised September 16, 1997.

The authors are with the Applied Physics Laboratory, Johns Hopkins University, Laurel, MD 20723 USA.

Publisher Item Identifier S 0018-926X(98)01047-3.

One approach to reducing the number of computing operations required to solve the rough surface scattering problem via method of moments is the banded matrix iterative approach (BMIA) [2]–[6]. The BMIA is based on splitting the field/surface current interaction into near (strong) and far (weak) components. A solution to the surface current is obtained by iteratively inverting the banded strong interaction matrix while updating (or correcting) the solution with the weak interaction (see Section III). In addition to the iterative solution, further savings are obtained by expanding the weak interaction about a canonical grid (CAG), the mean flat surface [2].

The BMIA/CAG method and a related approach, the sparse matrix flat-surface iterative approach (SMFSIA), have been successfully applied to scattering from one-dimensional (1-D) and 2-D random rough surfaces with rms heights comparable to or smaller than the incident wavelength. However, at microwave radar wavelengths (several millimeters to about one meter), rms heights for fully developed seas can be significantly larger. Under these conditions, we have found the BMIA to be of limited use. Through extensive calculations, it is shown (Section IV) that the iterative approach frequently fails to converge or converges to an incorrect solution. This behavior has a simple explanation. The weak interaction requires that two points on the surface have a much larger separation along the mean plane than off of the mean plane. The minimum weak-interaction distance ($r_d$) along the mean plane therefore grows with the surface height. For the typical radar-ocean problem, the value of $r_d$ required to avoid convergence problems is so large relative to the total surface length in the simulation that little or nothing is gained by splitting the interaction.

Since our objective is to simulate low-grazing-angle ocean radar scatter, we investigate alternative methods for improving the efficiency of the full-matrix method of moments solution. Our approach (described in Sections II and III) begins with a decomposition of the computational domain into multiple overlapping grids. The multigrid method has been extensively applied in computational fluid dynamics [7], [8]. The solution on each computational grid is accelerated by a generalized conjugate residual (GCR) method. This approach, while not as efficient as the BMIA/CAG with small interaction distance, is considerably faster than direct solution by LU decomposition and has the added benefit of a significant reduction in memory (some quantitative comparisons are made in Section V). Like the BMIA/CAG, the multigrid GCR method is, in principle, an exact solution to the moment method, but with no limitations

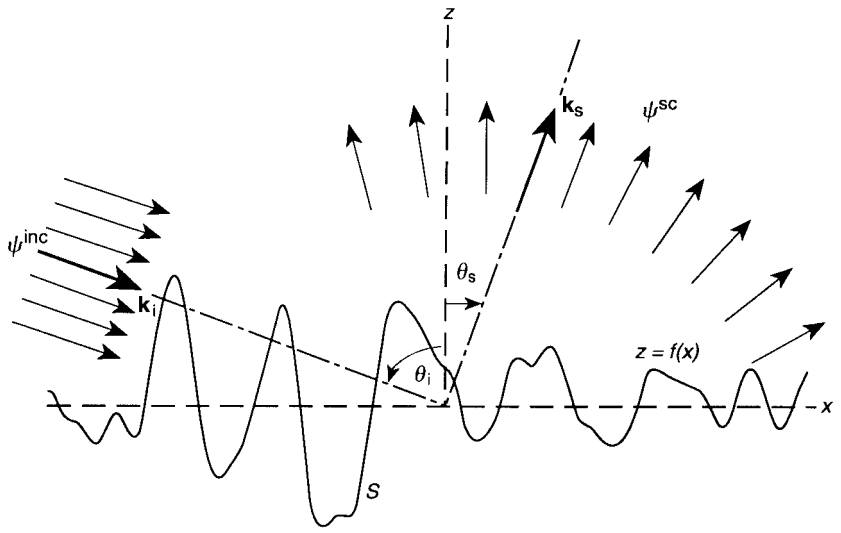


Fig. 1. Coordinate system and geometry for modeling wave scattering from a 1-D randomly rough surface. The rough surface $S$ is described by the height $z = f(x)$ above the mean plane.

on surface height. In this paper, we apply the method to scattering of horizontal and vertical polarized radar from perfectly conducting realizations of the ocean. The realizations are generated by a well-known spectral method [12] with a wind-dependent spectrum spanning the gravity to capillary wave ranges [13]. Particular attention is paid to backscattering and low-grazing angles.

## II. Method of Moments Formulation

This section describes the structure of the interaction matrix and, for the BMIA, the decomposition into strong and weak components. We consider both horizontal (Dirichlet) and vertical (Neumann) polarized electric fields incident on a perfectly conducting surface.

### A. Dirichlet (H-pol)

For this case, we follow the derivation given in Tsang *et al.* [2]. The starting point is the surface current integral equation for a field $\Psi^{\rm inc}$ incident on the rough surface

$$0 = \Psi^{\rm inc}(\mathbf{r}) - \int_S dx' G(\mathbf{r}, \mathbf{r}') u(\mathbf{r}') \quad \mathbf{r}, \mathbf{r}' \text{ on } S \tag{1}$$

where the integration (source point) is over the surface $S$ $r' = x'\hat{x} + f(x')\hat{z}$. The source function $u$ contains the surface current

$$u(\mathbf{r}') = \sqrt{1 + \left[\frac{df(x')}{dx'}\right]^2} \frac{\partial \Psi(\mathbf{r}')}{\partial n'} \tag{2}$$

where $\Psi$ is the *total* field (incident + scattered). The 2-D free-space Green's function is given by

$$G(\mathbf{r}, \mathbf{r}') = \frac{i}{4} H_0^{(1)}(k|\mathbf{r} - \mathbf{r}'|) \tag{3}$$

where $H_0^{(1)}$ is the Hankel function of the first kind order zero, and $k(= 2\pi/\lambda)$ is the free-space wavenumber. Note that the integration in (1) is over the mean plane ($z = 0$), hence, the Jacobian ($\sqrt{1 + f'^2}$) is included in (2). Also note that for this paper, we consider only the 2-D ($x$, $z$) scattering problem (Fig. 1).

Using (3), the surface-current integral equation may be written as a sum of two integral terms

$$\begin{aligned}\Psi^{\rm inc}(\mathbf{r}) &= \int_{-\infty}^{\infty} dx' \frac{i}{4} H_0^{(1)}(k\sqrt{[x - x']^2 + [f(x) - f(x')]^2}) \\ &\cdot u(x') U(r_d - |x - x'|) \\ &+ \int_{-\infty}^{\infty} dx' \frac{i}{4} H_0^{(1)}(k\sqrt{[x - x']^2 + [f(x) - f(x')]^2}) \\ &\cdot u(x') U(|x - x'| - r_d)\end{aligned} \tag{4}$$

where $U(x)$ is the heaviside step function. The first integral term in (4) corresponds to strong interaction between source and field point ($|x - x'| < r_d$), while the second term corresponds to weak interaction ($|x - x'| > r_d$). It is expected that due to the asymptotic behavior of the Hankel function, the strong interaction dominates the solution for $u$.

According to the method of moments, (4) is discretized and becomes

$$\mathbf{ZX} = \mathbf{C} \tag{5}$$

where the unknown column vector $\mathbf{X}$ discretizes the source function $u$ and $\mathbf{C}$ is the discretization of the incident field. For these calculations, we use the simplest discretization consisting of the point matching method with pulse basis functions [1]. For the BMIA, the interaction matrix $\mathbf{Z}$ is split into strong and weak components, i.e., $\mathbf{Z} = \mathbf{Z}^{(s)} + \mathbf{Z}^{(w)}$ where the strong matrix can be taken directly from (4),

$$Z_{i,j}^{(s)} = \begin{cases} \dfrac{i\Delta}{4} H_0^{(1)}(k\sqrt{[x_i - x_j]^2 + [f_i - f_j]^2}) & 0 \le |i - j| \le R_d \\ \dfrac{i\Delta}{4} H_0^{(1)}\left(\dfrac{k\Delta}{2e}\sqrt{1 + f_i'^2}\right) & i = j \\ 0 & |i - j| > R_d \end{cases} . \tag{6}$$

The quantity $\Delta$ is the sampling interval and we have $x_i = i\Delta$, $f_i = f(x_i)$, $f_i' = df(x_i)/dx$, and $R_d\Delta = r_d$. The self-impedance or diagonal term ($i = j$) is obtained by integrating the Hankel function over a small neighborhood about $x_i$ and using a first-order Taylor series expansion for the surface height $f(x_j)$.

For the weak interaction matrix, Tsang *et al.* [2] assume that the ratio $|f_i - f_j|/|x_i - x_j|$ is much less than one. This will always be true provided the strong interaction distance $r_d$ is sufficiently large compared to the maximum surface height. Under this assumption, the Hankel function may be approximated by a truncated Taylor series expansion about the mean plane or canonical grid. The expansion has the form

$$H_0^{(1)}(k\sqrt{[x_i - x_j]^2 + [f_i - f_j]^2}) = \sum_{m=0}^{M} a_m(|x_i - x_j|)\left[\left|\frac{f_i - f_j}{x_i - x_j}\right|^2\right]^m. \tag{7}$$

For the calculations shown in Sections IV–VI, a minimum of five expansion terms ($M = 4$) are used.

The iterative solution of (5) (discussed in Section III) involves products of the weak interaction matrix with successive iterations of the unknown vector $\mathbf{X}$. With the expansion shown in (7), the weak interaction matrix becomes a sum of matrices, each of which may be written as a translationally invariant matrix that is pre- and post-multiplied by diagonal matrices. Because of its cyclical symmetry (matrix elements depend only on the difference $|i - j|$), the product of a column vector with the translationally invariant matrix may be computed in order $N \log(N)$ operations. Reducing this product from order $N^2$ operations to order $N \log(N)$ is one of the key features of the BMIA/CAG method. It must be noted, however, that the iterative solution of (5) also requires an inversion of the banded strong interaction matrix; thus, the key feature of the BMIA/CAG can only be exploited in cases where the bandwidth ($R_d$) of the strong interaction remains small compared to the total problem size ($N$). This requirement imposes practical limitations that are further examined in Sections IV and V.

### *B. Neumann (V-pol)*

The surface current integral equation for a Neumann field is

$$\Psi(\mathbf{r}) = \Psi^{\text{inc}}(\mathbf{r}) + \int_S dS'\, \Psi(\mathbf{r}')\frac{\partial G(\mathbf{r}, \mathbf{r}')}{\partial n'} \qquad \mathbf{r}, \mathbf{r}' \text{ on } S \tag{8}$$

where $\Psi$ is again the total field and $\partial/\partial n'$ denotes the gradient normal to the surface. The normal gradient of the 2-D Green's function (3) is given by

$$\frac{\partial G(\mathbf{r}, \mathbf{r}')}{\partial n'} = \frac{-ik}{4}\frac{H_1^{(1)}(k|\mathbf{r} - \mathbf{r}'|)}{|\mathbf{r} - \mathbf{r}'|}\left(\frac{f'(x - x') - (z - z')}{\sqrt{1 + f'^2}}\right). \tag{9}$$

Note that unlike (1), the integration in (8) is written in terms of surface coordinates. The transformation between the surface and mean plane is given by

$$dS' = dx'\sqrt{1 + f'^2}. \tag{10}$$

Combining (8)–(10), and discretizing as in (6), the off-diagonal terms of the interaction matrix for vertical polarization become

$$Z_{i,j} = \frac{-ik\Delta}{4}\frac{H_1^{(1)}(k\sqrt{[x_i - x_j]^2 + [f_i - f_j]^2})}{\sqrt{[x_i - x_j]^2 + [f_i - f_j]^2}} \cdot [(f_i - f_j) - f_j'(x_i - x_j)] \qquad i \neq j. \tag{11}$$

Unlike the Dirichlet case (6), the interaction matrix is nonsymmetric due to the term $f_j'$. The Hankel function $H_1^{(1)}$ may be expanded about the canonical grid under the assumption $|f_i - f_j|/|x_i - x_j| \ll 1$ or weak interaction. The weak interaction matrix is then made cyclically symmetric by absorbing the nonsymmetric term $f_j'$ into the unknown $u_j$. The product of the symmetric weak interaction matrix with the modified unknown vector may then be computed in order $N \log(N)$ operations as for horizontal polarization.

For the diagonal or self-impedance term, we first recognize that the singularity at $\mathbf{r} = \mathbf{r}'$ in the scattered field integral of (8) contributes a term that is proportional to the total field $\Psi$, which, in this case, does not vanish on the scattering surface. After integrating out the singularity, the integral equation (8) becomes [9]

$$\tfrac{1}{2}\Psi(\mathbf{r}) = \Psi^{\text{inc}}(\mathbf{r}) + \int_S dS'\Psi(\mathbf{r}')\frac{\partial G(\mathbf{r}, \mathbf{r}')}{\partial n'} \qquad \mathbf{r}, \mathbf{r}' \text{ on } S \tag{12}$$

where the integration is now the principal value type. The self-impedance term is now calculated by integrating over the coincident field and source element ($i = j$), taking the field $\Psi$ to be fixed. This integral requires a second-order Taylor series expansion of the surface height $f(x_i)$ and an additional first-order expansion of the slope $f'(x_i)$. Using (9), (10), and (12) with the appropriate expansions, we obtain

$$Z_{i,i} = \frac{1}{2} - \frac{\Delta f_i''}{4\pi(1 + f_i'^2)} \tag{13}$$

which, along with (11), completes the derivation of the interaction matrix for vertical polarization.

### *C. Scattering Cross Section*

The numerical method outlined above is applied in this paper to calculating the normalized scattering cross-section of the rough surface. For the incident field, we use the well-known tapered plane wave [12]

$$\Psi^{\text{inc}}(\mathbf{r}) = e^{i\mathbf{k}\cdot\mathbf{r}[1 + W(\mathbf{r})]}e^{-(x + z\,\tan\,\theta_i)^2/g^2} \tag{14}$$

where

$$W(\mathbf{r}) = \frac{2(x + z\,\tan\,\theta_i)^2/g^2 - 1}{(kg\,\cos\,\theta_i)^2} \tag{15}$$

and $g$ is a length scale that determines the taper of the incident wave. For most calculations, we set $g = L/4$, where $L$ is the total length of the scattering surface. With this choice of incident field, it has been shown [2] that the normalized far-field scattering cross section for the Dirichlet problem is given by

$$\sigma_H(\theta_s) = \frac{\left| \int_{-\infty}^{\infty} e^{-ik[\sin\,\theta_s + \cos\,\theta_s f(x)]} u(x)\,dx \right|^2}{8\pi g k \sqrt{\pi/2}\,\cos\,\theta_i \left(1 - \dfrac{1 + 2\,\tan^2\,\theta_i}{2k^2 g^2\,\cos^2\,\theta_i}\right)}. \quad (16)$$

From (4) and (5), the source function $u$ is given in discrete form by the elements of the column vector $\mathbf{X}$. In Section V, we show that the calculation of (16) is, in some cases, sensitive to the choice of numerical integration rule.

For the Neumann problem, the equivalent definition of the normalized scattering cross section is given by (17), shown at the bottom of the page. In this case, the source function or total field $\Psi$ on the scattering surface is again given in discrete form by the elements of the column vector $\mathbf{X}$.

## III. Iterative Solution

We present two approaches for the iterative solution of (5). In approach I, the solution is generated on a single grid containing the total number of discretized points $N$. In approach II, the solution is generated on a sequence of grids from the finest grid with grid space $\Delta$ to the coarsest grid with grid space $2^p\Delta$ ($p$ is the grid level). Approach II is particularly attractive for a large number of unknowns [$N > O(10^4)$].

### A. Single-Grid Method

Here, we introduce the preconditioning method, which consists of solving an approximate problem whose solution can be easily related to that of the original problem. In place of (5), we solve

$$\tilde{\mathbf{Z}}^{-1}\mathbf{Z}\mathbf{X} = \tilde{\mathbf{Z}}^{-1}\mathbf{C}. \quad (18)$$

An iterative solution to (18) is given by

$$\tilde{\mathbf{Z}}\mathbf{X}^{n+1} = \tilde{\mathbf{Z}}\mathbf{X}^n + \alpha(\mathbf{C} - \mathbf{Z}\mathbf{X}^n) \quad (19)$$

where $n$ is the iteration number, $\alpha$ is a free parameter whose optimal value is described in the Appendix, and $\tilde{\mathbf{Z}}$ is a preconditioner. A good preconditioner often requires: 1) less memory and inexpensive effort to invert the resulting matrix and 2) a fast convergence rate. Fast convergence requires that the preconditioner should be close to the original operator $\mathbf{Z}$, i.e., the spectral condition number $\kappa$, the ratio of the maximum and minimum eigenvalues of $\|\tilde{\mathbf{Z}}^{-1}\mathbf{Z}\|$, should not be large. Here $\|\cdot\|$ is the standard $\ell_2$ Euclidean norm. One possible choice for $\tilde{\mathbf{Z}}$ that meets this requirement is the strong interaction matrix, i.e., $\tilde{\mathbf{Z}} = \mathbf{Z}^{(s)}$. With this choice, it can be shown that the method of successive substitution proposed by Tsang *et al.* [2] is a special case of the preconditioning method where $\alpha = 1$. However, in addition to the choice $\tilde{\mathbf{Z}} = \mathbf{Z}^{(s)}$ and $\alpha = 1$, the BMIA/CAG also approximates the residual $\mathbf{r} = \mathbf{C} - \mathbf{Z}\mathbf{X}$ by $\mathbf{r} \approx \mathbf{C} - (\mathbf{Z}^{(s)} + \mathbf{Z}^{(w)})\mathbf{X}$, where $\mathbf{Z}^{(s)} + \mathbf{Z}^{(w)}$ differs from the original operator $\mathbf{Z}$ when retaining a finite number of terms in the CAG expansion. It is demonstrated in Sections IV and V that when applied to large-amplitude rough surfaces, the BMIA/CAG may converge to an incorrect solution because of the approximation error in the residual. For calculations in this paper, a preconditioning approach based on (19) is used without approximating the residual, thereby avoiding convergence errors.

The inverse of the preconditioner $\tilde{\mathbf{Z}}$ in (19) can be determined by standard LU decomposition; that is, a one-time forward sweep requiring order $b^2N/2$ operations where $b(< N)$ is the bandwidth of the preconditioner. The stored matrix is then repeatedly used for backward substitution. The more efficient and well-known conjugate gradient method can also be applied, however, this method is best suited to a positive definite (symmetric/Hermitian) operator, which is not the case for either polarization. Another popular method, the generalized minimal residual (GMRES) [10], is valid for both symmetric and nonsymmetric systems. The GMRES method has a fast convergence rate, but requires a huge storage space. A variation called restarted GMRES can reduce the storage requirement, however, this method requires storage of previous iterations, which would become very expensive in a three-dimensional scattering model because of the large number of unknowns. For the calculations in this paper, we use the generalized conjugate residual (GCR) method [11] as our iterative scheme. This method, described in the Appendix, is rapidly convergent for both symmetric (H-pol) and nonsymmetric (V-pol) systems.

The preconditioned GCR method on a single grid is a more general form of the BMIA, which has been successfully applied to rough surfaces with rms heights comparable to or smaller than the incident wavelength. For larger surface heights, however, the GCR method with a preconditioned operator of reduced bandwidth $b$ (as in the BMIA) cannot guarantee convergence unless the bandwidth is significantly increased (see calculations in Sections IV and V below). This results in a tremendous storage requirement of $Nb$ for H-pol and $2Nb$ for V-pol and it slows the solution considerably. An alternative method for reducing the storage space and

$$\sigma_V(\theta_s) = \frac{k\,\cos^2\,\theta_s \left| \int_{-\infty}^{\infty} e^{-ik[\sin\theta_s + \cos\,\theta_s f(x)]}[1 - f'(x)\,\tan\,\theta_s]\Psi(x)\,dx \right|^2}{8\pi g\sqrt{\pi/2}\,\cos\,\theta_i \left(1 - \dfrac{1 + 2\,\tan^2\,\theta_i}{2k^2 g^2\,\cos^2\,\theta_i}\right)} \quad (17)$$

improving the convergence while retaining the preconditioned GCR approach is now described.

### *B. Multigrid Method*

The objective of the multigrid method [14], [15] is to remedy the deficiency of the traditional single-grid method. For elliptic problems such as the Helmholtz equation, during the iteration on a single grid, high-frequency errors with short wavelength comparable to the mesh size are quickly damped (smoothed), but low-frequency errors with long wavelength stay intact [16]. That is why most iterative schemes work very well for the first several iterations and then tend to slow toward convergence. The multigrid method enables us to efficiently remove the low-frequency errors by projecting them to a coarser grid on which the errors become more oscillatory and, thus, are more amenable to iterative schemes. The solution is generated on a sequence of grids spanning the finest grid spacing $\Delta$ to the coarsest spacing $2^p\Delta$ where $p$ is the grid level. The decomposition into multiscale grids is ideally suited to ocean scatter where the sea surface spectrum spans many scales of roughness.

To develop the multigrid solution, first define $\mathbf{r}_0 = \mathbf{C} - \mathbf{Z}_0\mathbf{X}_0$, which corresponds to the residual on the finest grid (the original problem). For calculations in this paper, we use the "standard coarsening," which involves doubling the mesh from one grid to the next coarsest grid and also smoothing the residual [$\mathbf{r} = f(\mathbf{r}_0)$, where $f$ stands for products of a sequence of operators] to the next coarsest grid (a process known as restriction [14], [15]). Whenever the problem is solved on the coarse grid (low-frequency or large-wavelength domain), the coarse-grid correction for the variable transfers the correction back (prolongation) to the fine grid (high-frequency or small-wavelength domain) to gain rapid convergence. Thus, the multigrid method can be viewed as a function to reduce the residual on the different frequency domains. The effect of the interaction among different grids is complementary. On the coarse grid (level $p+1$), the equation solved is an improved approximation to the solution on the fine grid (level $p$) where the error components are smoothed. The fine grid solution, in turn, provides a more accurate projection of low-frequency errors to the coarse grid.

The interaction between the fine grid and the coarse grid can be symbolically correlated by

$$\mathbf{Z}_{p+1}\mathbf{X}_{p+1} - \mathbf{Z}_{p+1}(\mathbf{I}_{p+1}^{p}\mathbf{X}_p) = \mathbf{I}_{p+1}^{p}\mathbf{r}_p. \tag{20}$$

Here, $\mathbf{Z}_{p+1}$ represents the operator of (5) on the coarse grid, $\mathbf{I}_{p+1}^{p}$ is an interpolation operator (restriction) from the fine grid "$p$" to the coarse grid "$p+1$" $\mathbf{X}_p$ is the unknown vector, and the residual $\mathbf{r}_p$ is defined as

$$\mathbf{r}_p = \mathbf{I}_{p}^{p-1}\mathbf{r}_{p-1} - \mathbf{Z}_p(\mathbf{X}_p - \mathbf{I}_{p}^{p-1}\mathbf{X}_{p-1}) \tag{21}$$

for $p > 1$ and $\mathbf{r}_1 = \mathbf{I}_1^0\mathbf{r}_0$. The left-hand side of (20) is the difference between the coarse-grid operator acting on the coarse grid and the coarse-grid operator acting on the interpolated fine grid (which is held fixed). After the fine-grid solution has converged, the residual $\mathbf{r}_p$ will be zero and the solution of (20) becomes

$$\mathbf{X}_{p+1} = \mathbf{I}_{p+1}^{p}\mathbf{X}_p \tag{22}$$

as required. When the residual is nonzero, the left-hand side of (20) acts as a forcing term for the coarse-grid correction and the correction to $\mathbf{X}_{p+1}$ must be transferred back (prolongated) to the fine grid, i.e.,

$$\mathbf{X}_p^{\text{new}} = \mathbf{X}_p^{\text{old}} + \mathbf{I}_{p}^{p+1}(\mathbf{X}_{p+1} - \mathbf{I}_{p+1}^{p}\mathbf{X}_p^{\text{old}}) \tag{23}$$

where the superscript "new" represents the updated information during the multigrid iterative solution. This is vital for the success of the scheme. Changes in the variables are transferred back to the fine grid rather than the variables themselves.

The coarse grid operator $\mathbf{Z}_p$ is a projection of the original operator $\mathbf{Z}$ onto the $p$th grid. For standard coarsening (doubling of the mesh size to the next grid level), the projection is straightforward. Assuming that $i_p$ and $j_p$ are the indexes of the mesh point on the $p$th level, the matrix element $\mathbf{Z}_{p_{i_p,j_p}}$ is given by the appropriate expressions for H-pol or V-pol [(6) or (11) and (13), respectively] with indexes given by

$$\begin{aligned} i &= 2^p(i_p - 1) + 1 \\ j &= 2^p(j_p - 1) + 1. \end{aligned} \tag{24}$$

In addition, the grid spacing $\Delta$ is replaced by $\Delta_p = 2^p\Delta$. Both $\mathbf{I}_{p}^{p+1}$, the prolongation operator from the coarse grid to the fine grid, and $\mathbf{I}_{p+1}^{p}$, the restriction operator from the fine grid to the coarse grid, can be simply constructed through linear interpolation [14].

The order in which the grids are visited is called the multigrid cycle or multigrid schedule. If the order is fixed in advance we have a fixed schedule; if the order depends on intermediate computational results we have an adaptive schedule. In this paper, we use a fixed schedule, either smoothing the residual to the lower coarse-grid level or transferring the coarse-grid correction to the upper fine-grid level. A complete cycle constitutes one multigrid iteration. For comparisons among different cycles (fixed schedule), e.g., "V," "W," "F," and "Sawtooth", the reader is referred to Wesseling [17]. The calculations in this article use the W-cycle (Fig. 2). For each multigrid iteration, the residual on the grid $p = 0$ is first smoothed and estimated, then restricted to the next finest grid level. In our case, the iterative solution of the surface current $\mathbf{X}$ by the four-grid ($M = 3$) W-cycle can be cast in the form

$$\begin{aligned} \mathbf{X}_0^{\text{new}} = \mathbf{X}_0^{\text{old}} &+ \mathbf{I}_0^1\mathbf{Z}_1^{-1}\mathbf{I}_1^2\mathbf{Z}_2^{-1}\mathbf{I}_2^3\mathbf{Z}_3^{-1}\mathbf{I}_3^2\mathbf{Z}_2^{-1}\mathbf{I}_2^3\mathbf{Z}_3^{-1}\mathbf{I}_3^2\mathbf{Z}_2^{-1}\mathbf{I}_2^1 \\ &\mathbf{Z}_1^{-1}\mathbf{I}_1^2\mathbf{Z}_2^{-1}\mathbf{I}_2^3\mathbf{Z}_3^{-1}\mathbf{I}_3^2\mathbf{Z}_2^{-1}\mathbf{I}_2^3\mathbf{Z}_3^{-1}\mathbf{I}_3^2\mathbf{Z}_2^{-1}\mathbf{I}_2^1\mathbf{Z}_1^{-1}\mathbf{I}_1^0 \\ &\cdot(\mathbf{C} - \mathbf{Z}_0\mathbf{X}_0^{\text{old}}) \end{aligned} \tag{25}$$

which clearly demonstrates the interactions between different grid levels. The residual is smoothed from grid level $p$ to $p+1$ by the restriction process (21), while the coarse-grid correction from grid level $p+1$ to $p$ is transferred by the prolongation process (23).

The correction terms for restriction $\mathbf{Z}_{p+1}^{-1}\mathbf{I}_{p+1}^{p}\mathbf{r}_p$ and for prolongation $\mathbf{Z}_p^{-1}\mathbf{I}_p^{p+1}\mathbf{r}_{p+1}$ require a matrix inverse, which can be obtained at each grid level by the preconditioned GCR method.

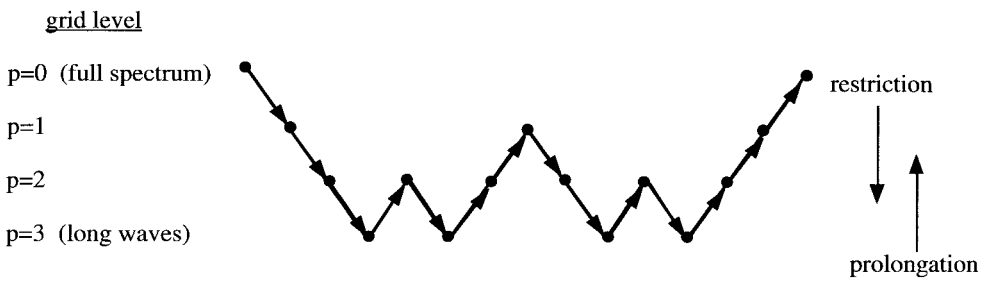


Fig. 2. Illustration of the four-grid ($M = 3$) W-cycle. The solution is first generated on the fine grid $p = 0$. Downward arrows represent restriction of the residual to the next finest grid level. Upward arrows represent prolongation of the coarse-grid correction. At any grid level, the terminus of an upward arrow is a "new," or updated solution. The corresponding "old" solution lies to the left along the same grid level.

This approach is crucial to the success of the algorithm, as it accelerates the convergence while also reducing the working space. With the definition $\Delta\mathbf{X}_{p+1} = \mathbf{X}_{p+1} - \mathbf{I}_{p+1}^{p}\mathbf{X}_p$, the iterative solution of (20) by the preconditioned GCR method has the form

$$\tilde{\mathbf{Z}}_{p+1}\Delta\mathbf{X}_{p+1}^{n+1} = \tilde{\mathbf{Z}}_{p+1}\Delta\mathbf{X}_{p+1}^{n} + \alpha(\mathbf{I}_{p+1}^{p}\mathbf{r}_p - \mathbf{Z}_{p+1}\Delta\mathbf{X}_{p+1}^{n}) \tag{26}$$

where $n$ is the iteration number at each grid level. The coarse grid operator $\mathbf{Z}_{p+1}$ is based on the grid spacing $\Delta_{p+1} = 2^{p+1}\Delta$. The preconditioned operator $\tilde{\mathbf{Z}}_{p+1}$ is formed by banding the coarse-grid operator $\mathbf{Z}_{p+1}$ as in the BMIA strong interaction. This reduces the number of operations required to invert $\tilde{\mathbf{Z}}_{p+1}$ and also requires a much smaller storage space than for $\mathbf{Z}_{p+1}$. On the finest grid, considerable savings can be attained by choosing a relatively small bandwidth for $\tilde{\mathbf{Z}}_{p+1}$. With the multigrid method, rapid convergence is still possible because the low-frequency error is quickly smoothed on the coarse grids (Section V and Fig. 7 discuss the convergence history). On the coarsest grid $M$, $\tilde{\mathbf{Z}}_M$ is either set equal to $\mathbf{Z}_M$ (no banding) or a large bandwidth is used to ensure that fast convergence can be reached. The number of operations and memory required here are minimal, since level $M$ is considerably smaller than the original problem (level 0). Note that with the choice $\tilde{\mathbf{Z}}_{p+1} = \mathbf{Z}_{p+1}^{(s)}$, we have a multigrid BMIA method. In this case, a canonical grid expansion (CAG) can be implemented on each grid level.

When the coarse-grid correction process transfers the correction from grid level $p+1$ to $p$, (26) can be written as

$$\Delta\mathbf{X}_p^{\text{new}} = \Delta\mathbf{X}_p^{\text{old}} + \mathbf{I}_p^{p+1}\Delta\mathbf{X}_{p+1}^{\text{old}} \tag{27}$$

for $p > 0$ and

$$\mathbf{X}_0^{\text{new}} = \mathbf{X}_0^{\text{old}} + \mathbf{I}_0^{1}\Delta\mathbf{X}_1^{\text{old}} \tag{28}$$

for $p = 0$. Note that the superscript "new" becomes "old" after updating the information according to (27) or (28). In the W-cycle diagram (Fig. 2), prolongation from a lower grid level is indicated by an upward arrow. The "new" solution is at the terminus of the upward arrow, while the corresponding "old" solution lies to the left, along the same grid level. Also note from this figure that the lower grids are visited several times during the course of one cycle. For one multigrid cycle, the coarse-grid correction process eventually transfers the correction back to the finest grid level $p = 0$. If the residual $\mathbf{r}_0$ does not meet the convergence criterion ($\|\mathbf{r_0}\| < \epsilon$), the multigrid iteration is repeated until the convergence check is satisfied.

## IV. BMIA/CAG Applied to Large-Amplitude Surfaces

We have developed a numerical code based on the moment-method formulation described in Section II and using the iterative solution techniques of Section III. As mentioned previously, the BMIA/CAG is a special case of our iterative procedure (19) with the choices $\mathbf{Z} = \mathbf{Z}^{(s)}$ and $\alpha = 1$ and with the residual $\mathbf{r} = \mathbf{C} - \mathbf{ZX}$ approximated by $\mathbf{r} \approx \mathbf{C} - [\mathbf{Z}^{(s)} + \mathbf{Z}^{(w)}]\mathbf{X}$. In this section, we consider the application of a multigrid BMIA/CAG to surfaces whose amplitudes exceed the incident wavelength. The BMIA/CAG results are compared with a more exact multigrid with GCR calculation, where no approximation has been made to the residual.

We first consider a sinusoidal surface described by

$$f(x) = h\,\sin\left(\frac{2\pi x}{\Lambda}\right) \qquad -L/2 < x < +L/2. \tag{29}$$

For perfect conductivity, the solution of a plane wave incident on the sinusoid has been studied for many years. Numerical solutions may be obtained by several different methods, however, with the exception of moment methods, all are limited by the Rayleigh criterion, i.e., $h < 0.448\Lambda/2\pi$ [18]. A set of moment method calculations for various ratios $h/\lambda$ and $\Lambda/\lambda$ for both H- and V-polarizations appear in Zaki and Neurether [19], [20]. Our numerical code has been compared with the numerical solutions shown in those papers. In all cases, excellent agreement was obtained. In addition, our numerical results are in agreement with an analytical theory [21] based on the Rayleigh plane wave expansion in the limit $h < \lambda$. For surface amplitudes exceeding the wavelength, no reference solutions exist. However, it is assumed that the convergence criterion $\|\mathbf{C}-\mathbf{ZX}\| < 10^{-4}$ is sufficient to guarantee accuracy, since the exact residual is used.

For these comparisons, the incident plane wave was simulated by setting the parameter $g$ in (14) to be much larger than the surface length $L$. The length was set to $L = 10\ \Lambda$ so that the normalized scattering cross section closely approximated that from an infinite periodic surface. To test the BMIA/CAG at large amplitude $h$, we consider only the specular cross section at H-pol, $\sigma_H(\theta_i)$. At other scattering angles, our numerical results reproduce the well-known Bragg scattering lobes. Calculations of the specular cross-section

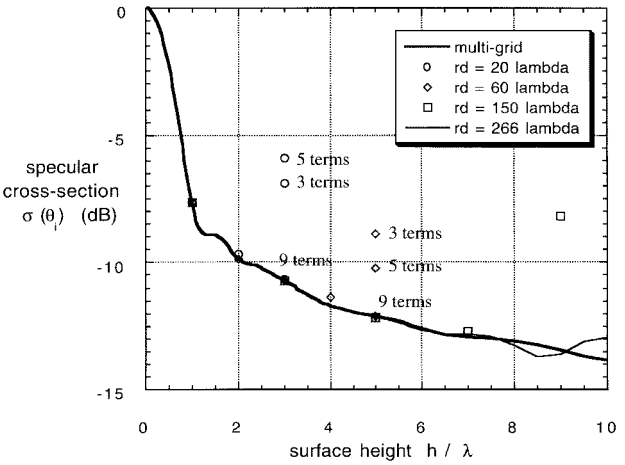


Fig. 3. Calculation of the specular cross section (H-pol) from a sinusoidal surface of period $\Lambda = 32.7\ \lambda$ and amplitude $h$ (29). The preconditioned GCR or reference solution is shown by the thick line. A set of converged BMIA/CAG solutions are shown for $r_d$ ranging from 20 to 266 $\lambda$. The total surface length is 327 $\lambda$, or ten periods ($N = 7848$).

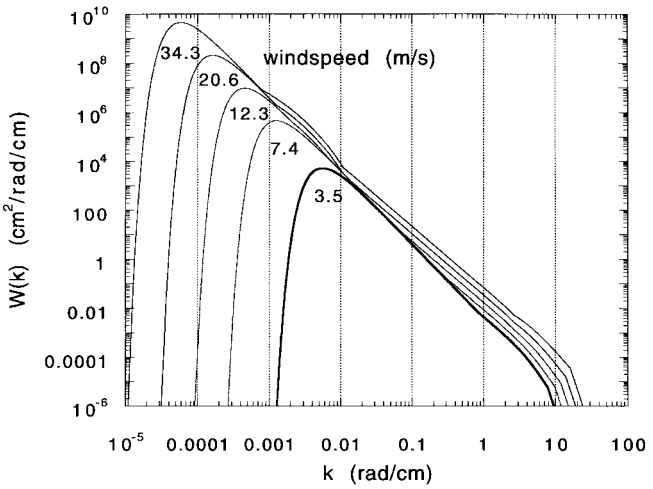


Fig. 4. Sample calculation of the direction-independent part of the Bjerkaas–Riedel sea-surface elevation spectrum for a variety of windspeeds.

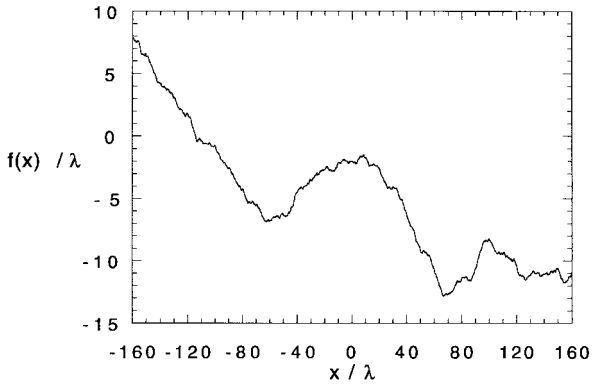


Fig. 5. Sample realization of the sea surface based on the Bjerkaas–Riedel spectrum with windspeed $u = 10$ m/s. The plot is normalized to a radar wavelength of 10 cm. The random surface realizations are generated by a spectral method [12].

from surfaces of $\Lambda = 32.7\ \lambda$ are shown in Fig. 3. The maximum surface amplitude calculated is $h = 10\ \lambda$, which is well beyond the Rayleigh cutoff of $h = 2.33\ \lambda$.

The thick solid line in Fig. 3 is calculated by multigrid (4-grid) preconditioned GCR without strong/weak decomposition and it is taken to be the reference solution for the calculation. The BMIA/CAG solution is then generated for bandwidth $r_d$ ranging from 20 $\lambda$, or less than one period, to 266 $\lambda$, which is a sizable fraction of the ten period surface ($L = 327\ \lambda$). It can be seen that for each choice of $r_d$, the BMIA result agrees with the reference solution to a maximum surface amplitude determined by the ratio $r_d/L$. The maximum surface amplitude is somewhat dependent on the number of terms retained in the canonical grid expansion. For example, the $r_d = 20\ \lambda$ calculation agrees with the reference solution at $h = 1\ \lambda$ and $h = 2\ \lambda$ using five expansion terms. At $h = 3\ \lambda$, nine terms are required. At $h = 4\ \lambda$ and beyond, the BMIA/CAG ($r_d = 20\ \lambda$) does not converge when 15 expansion terms are used. The behavior is similar for $r_d = 60\ \lambda$. In this case, an accurate solution is obtained at $h = 5\ \lambda$ by including nine expansion terms. However, the method will not converge with 15 expansion terms for $h = 6\ \lambda$ and beyond. We emphasize again that each of the BMIA/CAG results shown in Fig. 3 is converged. However, because of the approximation made to the residual by the canonical grid expansion, many of the results are numerically incorrect. At larger amplitudes beyond those shown for each $r_d$, the algorithm will not converge, even with a large number of expansion terms.

A second test of the BMIA/CAG was conducted on random ocean surface realizations. The realizations were generated using the spectral technique [12] with a Gaussian normal height probability density function (pdf) and a direction-independent sea-surface elevation spectrum [13]. The windspeed dependent Bjerkaas–Riedel spectrum is a composite of five spectral ranges, from long-wavelength gravity waves (Pierson–Moskowitz range) to short-wavelength capillary waves (Mitsuyasu–Honda range) and viscous dissipation (Cox viscous cutoff range). A plot of the direction-independent spectrum at various windspeeds is shown in Fig. 4. Fig. 5 is a sample realization of the ocean surface model for windspeed $u = 10$ m/s. The plot is shown normalized to a 10-cm radar wavelength. For this particular realization, the rms surface height is 7.23 $\lambda$ and the maximum peak-to-trough height differential is about 21 $\lambda$. It should be noted that the dominant contribution to the wave amplitude comes from wave components near the long-wavelength peak of the spectrum, shown in Fig. 4. Unlike the typical Gaussian rough surface with Gaussian spectrum, the sea surface consists of small-scale roughness superimposed on long-wavelength structures with amplitudes that are typically much larger than the incident radar wavelength.

A calculation of the normalized scattering cross section of the surface shown in Fig. 5 is plotted in Fig. 6. The cross section is shown as a function of scattering angle for a fixed incidence angle of 82° and for the 10-cm radar wavelength. The preconditioned GCR solution (thick line) is compared with the BMIA/CAG solution using $r_d = 140\ \lambda$ or 7/16 $L$ and $M = 4$ expansion terms. At some angles, the error is as large as a factor of two. It is clear that

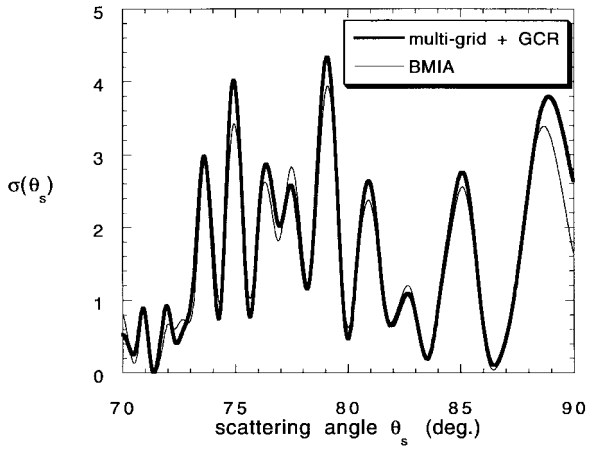


Fig. 6. Calculation of the normalized scattering cross section (H-pol) from the surface shown in Fig. 5 ($N = 7680$). The incidence angle is 82° and the plot shows a narrow range about the specular direction. The preconditioned GCR solution (thick line) is compared with a BMIA/CAG calculation using $r_d = 7/16L$.

TABLE I
COMPUTATIONAL PERFORMANCE ON A SAMPLE SEA SURFACE ($N = 12\,000$)

| Method | Storage (MB) | CPU time (min) | $\| \mathbf{C} - \mathbf{Z}\bar{\mathbf{X}} \|$ ($\leq 10^{-4}$) | iterations or cycles | energy integral |
|---|---|---|---|---|---|
| LU | $2.30 * 10^3$ | huge | machine limit | 1 | |
| BMIA/CAG (5 term, $b \leq 6000$) | $1.15 * 10^3$ | | not converged | | |
| BMIA/CAG (15 term, $b \leq 6000$) | $1.17 * 10^3$ | | not converged | | |
| BMIA/CAG (5 term, $b = 7000$) | $1.34 * 10^3$ | 576 | 4.406 | 21 | 1.00984 |
| BMIA/CAG (15 term, $b = 7000$) | $1.36 * 10^3$ | 624 | $3.07 * 10^{-3}$ | 22 | 0.99985 |
| single-grid GCR | 35 | 743 | $7.88 * 10^{-5}$ | 32 | 0.99985 |
| multi-grid GCR | 33 | 761 | $9.22 * 10^{-5}$ | 8 | 0.99985 |
| single-grid GCR | 10 | 1150 | $8.62 * 10^{-5}$ | 50 | 0.99985 |
| multi-grid GCR | 10 | 1024 | $9.12 * 10^{-5}$ | 10 | 0.99985 |

for a windspeed of 10 m/s, with 10-cm wavelength, the minimum bandwidth for the BMIA/CAG exceeds 140 $\lambda$ or 14 m and this minimum will increase with windspeed. Fig. 3 demonstrates that the minimum bandwidth may be decreased somewhat by adding expansion terms, however, one must also consider the additional CPU time (see Table I). With the minimum weak interaction distance so large, the BMIA apparently offers little advantage, unless one considers very large surfaces on the order of 1000 $\lambda$ (100 m) or more. With the possible exception of incidence angles within a few degrees of grazing, there is generally no reason to consider such a large surface, particularly since the dominant wavelength in the ocean spectrum (for wind speed of 10 m/s) is on the order of 91 m. Moreover, the computing time and memory requirement for surfaces of that size are mostly impractical, particularly for Monte Carlo calculations.

We note that the same calculation as shown in Fig. 6 was repeated on a single realization at $u = 4$-m/s windspeed (rms height = 1.15 $\lambda$). In this case, there was no discernible difference between the preconditioned GCR and BMIA/CAG solutions. We, therefore, conclude that for ocean-radar scatter, the BMIA/CAG may only be practical for very light winds and wavelengths on the order of 10 cm or larger. In many such cases, approximate methods requiring far less computing time may be adequate.

## V. COMPUTATIONAL PERFORMANCE OF THE MULTIGRID + GCR APPROACH

To provide a measure of the relative efficiency and accuracy of the multigrid and GCR solutions, the method is applied to scattering from a single realization of the Bjerkaas–Riedel spectrum with wind speed equal to 10 m/s. The incident wavelength is 3 cm and incidence angle equals 80°. The surface is sampled with 20 points per wavelength and is 600 wavelengths long for a total of $N = 12\,000$ unknowns. Table I compares storage and CPU requirements for several different methods applied to the same surface realization. The table also lists the exact residual achieved by each method at convergence and, for energy conservation, the integral of the normalized cross section over scattering angle. The number of iterations or multigrid cycles required for each method is also listed.

Starting from the top of Table I, we find the storage requirement for a full-matrix (LU) solution exceeds the computers available to us. Given the number of operations required, the CPU time should also be extremely large. We found the BMIA was unable to converge for bandwidth $b \leq 6000$ unknowns as a result of the approximation error in the residual. The storage requirement for $b = 6000$ is also too large for our computers. To reduce storage, the BMIA calculations were performed with a preconditioned operator, which is numerically equivalent but prevented us from determining cpu time for a true BMIA calculation (note BMIA/CAG CPU times are with a precondition operator, while storage is without). The BMIA did converge for $b = 7000$, however, for five expansion terms the exact residual was very large. Note that the exact residual is a one-time calculation done for comparison and it is not part of the BMIA. A single grid with preconditioned GCR calculation required only 35 MB of storage and converged to a small residual in 32 iterations. The multigrid/GCR method with comparable storage required only eight cycles, however, because the cycle is more expensive than a single-grid iteration, CPU time was comparable. The real benefit of the multigrid approach can be seen in the last example, where memory for the problem with 12 000 unknowns was reduced to only 10 MB by choosing a very small bandwidth for the preconditioner. In this case, the single-grid calculation required 50 iterations and 1150 CPU min. Because of its improved convergence properties, the multigrid calculation required only ten cycles and 1024 CPU min. This result demonstrates that the multigrid approach will be particularly attractive for problems where an extremely large number of unknowns (as for three dimensions) must be solved with reasonable memory requirements.

The improved convergence properties of the multigrid approach are also illustrated in Fig. 7. The scattering is again calculated from a single realization of the Bjerkaas–Riedel

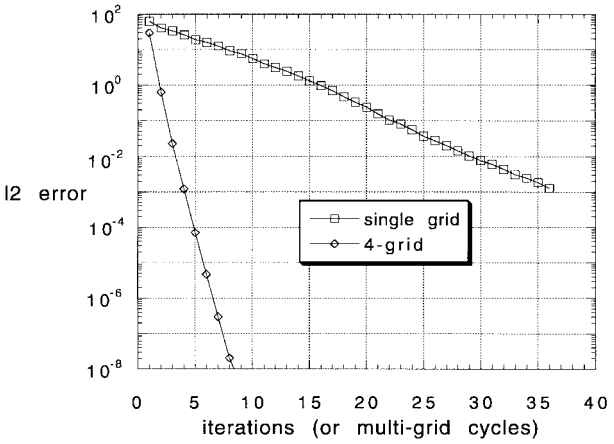


Fig. 7. Calculated residual error ($\ell_2$ norm) as a function of iteration number (single-grid method) or multigrid cycle (four-grid method) for a sample sea surface with wind speed equal to 10 m/s.

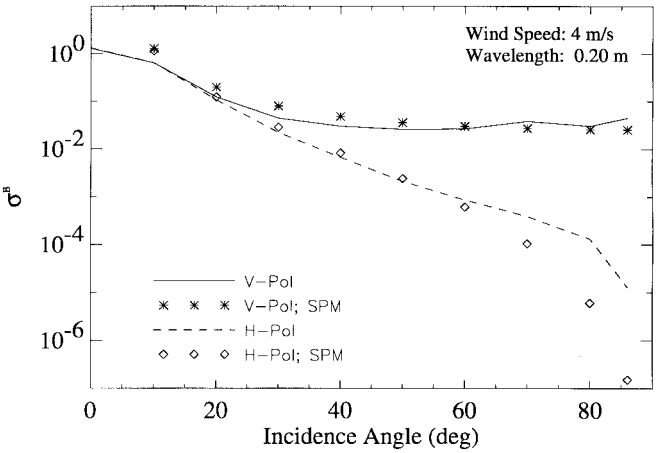


Fig. 8. Multigrid calculation of the backscatter cross section from random sea surface realizations ($L = 360\ \lambda$, $N = 7200$). The radar wavelength is 20 cm and windspeed is 4 m/s. The results are an average of 80 realizations. The SPM solution (30) is also shown.

spectrum (windspeed = 10 m/s). The incident wavelength is 3 cm, and the problem is computed with $N = 7200$ unknowns. The bandwidth of the preconditioner on the fine grid is set to a relatively small $b = 100$ unknowns. Because of the persistence of low-frequency errors, the single-grid iterative approach converges very slowly. Faster single-grid convergence is obtained by increasing the bandwidth and, hence, the computing time and storage requirement. The four-grid approach, in contrast, reduces the residual error to the required $10^{-4}$ in only five iterations. In this case, faster convergence can be obtained (to a limit) by introducing additional coarse-grid levels, without affecting the bandwidth. Since the coarse-grid problem is considerably smaller, the additional computation is minimal.

## VI. Sea Scattering Results

In this section, we use the multigrid (four-grid) with GCR method (Section III) to calculate polarized scatter from random realizations based on the Bjerkaas–Riedel sea spectrum. Because of the limitations discussed above, no splitting of the interaction matrix into strong and weak components is employed. Particular attention is paid to the difficulties encountered with very low-grazing-angle scatter, regardless of the solution method.

For low windspeeds, the small perturbation method (SPM) is often used to approximate ocean-radar backscatter. It can be shown that for a 1-D rough surface, the normalized backscatter cross section reduces to [22]

$$\sigma_{SPM}(-\theta_i) = 4\pi k^3 \begin{bmatrix} \cos^4\theta_i & \text{Hpol} \\ (1+\sin^2\theta_i)^2 & \text{Vpol} \end{bmatrix} W(2k\sin\theta_i) \quad (30)$$

where $W$ is the one-sided surface spectrum. This result may be calculated from the Bjerkaas–Riedel spectrum and compared with numerical results. In Fig. 8, a comparison is made for a 4-m/s wind and 20-cm radar wavelength. The numerical results are based on surface lengths of 90–360 $\lambda$ and the results are averaged over 80 realizations.

At low and moderate incidence angles the agreement is quite good. At incidence angles beyond 70°, the numerical results at V-pol slightly exceed the SPM. The error is mostly uniform out to the limit of 86°. The most prominent differences are in the low-grazing-angle H-pol results, particularly in the range $70° < \theta_i < 86°$. There is apparently a problem with the very small ratio of backscattered to total scattered energy. A normalized backscatter cross-section in the range $10^{-4} < \sigma_B < 10^{-3}$ represents an effective "noise-floor" for the calculation. At higher windspeeds, the backscatter cross-section approaches the noise floor only at the very lowest grazing angles and only for H-pol. Nevertheless, a more accurate calculation under these conditions would be desirable.

We have found that for these very small backscatter cross sections (low-grazing angle), the result is highly sensitive to the numerical rule used to integrate the surface current (16). For the calculations shown in Fig. 8, a third-order polynomial extrapolation (equally spaced) was used. Higher order polynomials offer no improvement and often generate slightly larger errors. It is also interesting to note that the accuracy of the backscatter calculation under these conditions is generally not quantifiable by testing for energy conservation. Theoretically, the integral of the normalized scattering cross section (16) over all scattering angles should equal one. In practice, however, the computed integral usually differs from one in the second or third decimal. Because the backscattered signal contributes negligibly to the total scattered power, order of magnitude calculation errors in $\sigma_B$ are not quantifiable by this measure.

Fig. 8 is taken to 4° grazing angle at both polarizations. Lower grazing angles become problematic for several reasons. One expects multiple scattering to become increasingly important in this limit and, in fact, we observe multiple scatter well outside of the directly illuminated area. Fig. 9, for example, is a plot of the induced surface current for an H-pol incident beam with 1/e diameter of 25 $\lambda$ and grazing angle of 10°. It can be seen that current is induced well outside of the directly illuminated area ($-12.5\ \lambda < x < 12.5\ \lambda$). As the grazing angle approaches zero and the illuminated area is

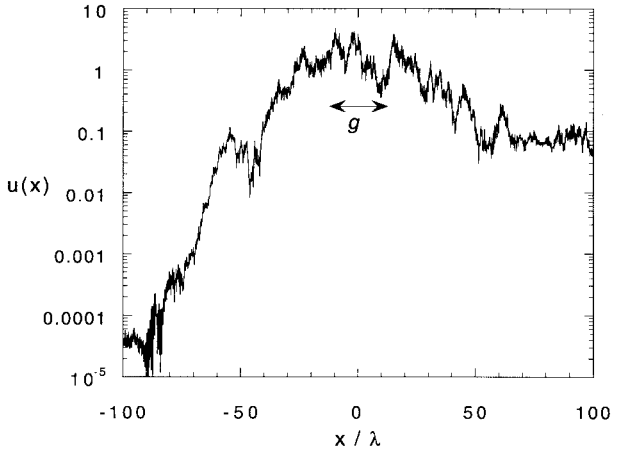


Fig. 9. Plot of the source function $u(x)$ (H-pol) from one realization of the surfaces averaged in Fig. 8. The incidence angle is 80° and the incident beam illuminates the area roughly shown by $g$, the $1/e$ scale of the beam.

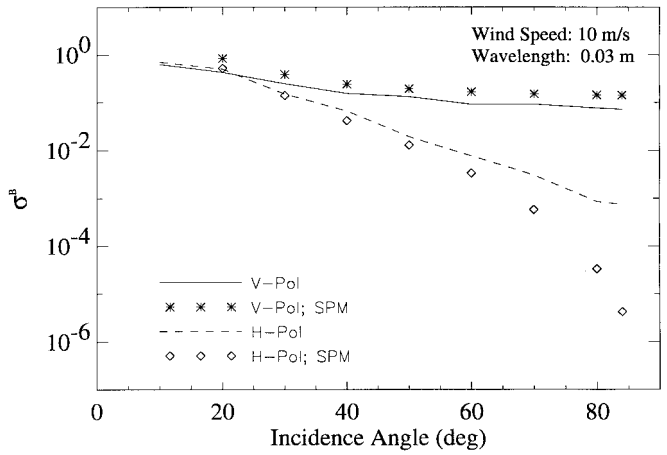


Fig. 10. Same as Fig. 8, but with 3-cm radar wavelength and 10-m/s windspeed.

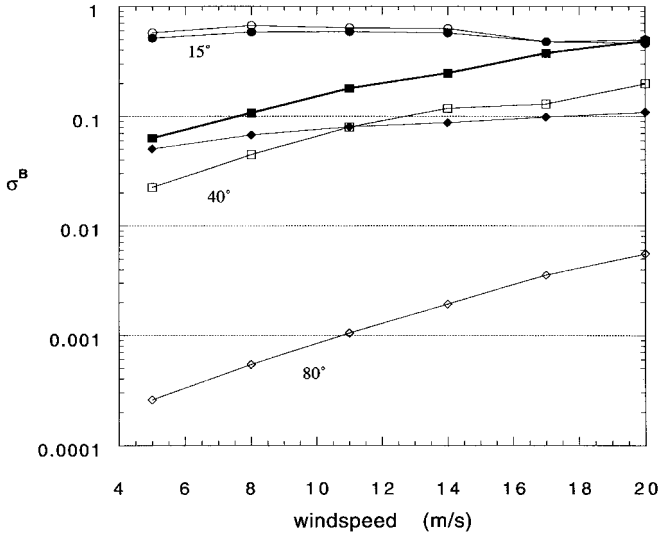


Fig. 11. Multigrid calculation of sea-surface backscatter as a function of windspeed ($L = 360\ \lambda$, $N = 7200$). Results are calculated for near-normal (15° circles), intermediate (40° squares), and near-grazing (80° diamonds) incidence angles. The open symbols show H-pol and solid symbols show V-pol. All results are for 3-cm radar wavelength.

held constant, the surface current covers an increasingly larger area, thereby requiring a larger computational domain for the scattering calculation. The smallest grazing angles in Fig. 8 are calculated for $L = 360\ \lambda$ compared to $L = 90\ \lambda$ from normal incidence to $\theta_i = 80°$.

The numerical calculation shown in Fig. 8 is repeated for Fig. 10, but with a windspeed of 10 m/s and 3-cm radar wavelength. For these parameters, the ratio of wave height to incident wavelength is much greater than one, so that the assumptions of perturbation theory (SPM) are no longer valid. Nevertheless, the numerical results again predict the V-pol backscatter to be very weakly dependent on incidence angle, particularly at larger incidence angles, in agreement with SPM. Compared to Fig. 8, where $u = 4$ m/s, the V-pol result is significantly larger, especially at moderate incidence angles. This is expected on physical grounds, since the Bragg resonant wavelength $\pi/(k \sin \theta_i)$ ranges from 4.38 cm at 20° incidence to 1.73 cm at 60° incidence and $\lambda = 3$ cm. In this range of length scales, the Bjerkaas–Riedel sea spectrum is strongly wind dependent [13]. The H-pol backscatter increases with wind as well, with the greatest differences between Figs. 8 and 10 occurring at large incidence angles.

The windspeed dependence is examined in detail in Fig. 11, which is again calculated for 3-cm radar wavelength. The low-grazing angle ($\theta_i = 80°$) H-pol result is the most strongly wind dependent. Interestingly, V-pol return at low-grazing angle is very weakly wind dependent, particularly for higher windspeeds. At 15° incidence, both polarizations in Fig. 11 are nearly independent of windspeed. An experimental confirmation of this result, based on data collected at 3 cm [24] and 2.15 cm [23] wavelengths, is reported in Wetzel [25]. At even smaller incidence angles, our results indicate a slight *decrease* in $\sigma_B$ with windspeed, which is expected since the increased small-scale roughness reduces specular reflection [26].

## VII. Summary

We have developed a general iterative numerical solution to the method of moments formulation of rough surface scattering. The method is developed for both horizontal (Dirichlet) and vertical (Neumann) polarized electric fields incident on perfectly conducting surfaces and there is no restriction on the amplitude of the rough surface relative to the incident wavelength. A key component of the method is a decomposition of the scattering problem into multiple overlapping grids, each corresponding to a different range of spatial frequencies or length scales. This approach is ideally suited to scattering from the ocean surface, which is shown by spectral models to encompass a broad range of length scales from long-wavelength gravity waves (tens or hundreds of meters) to short wavelength capillary waves (millimeters). Compared to numerical solution by full-matrix inversion, the multigrid iterative method substantially reduces the computing time and can reduce computer memory to a small fraction (by introducing additional grid levels and reducing the size of the preconditioning matrix).

A previously introduced iterative method, the BMIA [2]–[4], is shown to be a special case of the multigrid method.

A multigrid form of the BMIA is applied to several sample problems, including the ocean surface at moderate windspeed and microwave radar wavelengths. Because the surface height in these problems greatly exceeds the radar wavelength, the BMIA is found to converge to an incorrect solution unless the strong matrix bandwidth encompasses most of the computational domain. Through extensive calculations, we find that the BMIA may only be practical for an appropriate combination of light winds and longer radar wavelengths. By choosing a sufficiently large number of grid levels and combining with the preconditioned GCR approach, the multigrid method can be applied to such problems with increased efficiency and no loss of numerical accuracy.

For ocean surface backscatter calculations, our numerical results demonstrate good agreement with perturbation theory out to low-grazing angles and we are able to apply the method at higher windspeeds and smaller wavelengths where the assumptions of perturbation theory are no longer satisfied. Numerical results are obtained to within 4° of grazing and, for V-pol, good agreement with perturbation theory is observed in the limit of small windspeed. At H-pol, however, numerical difficulties are encountered. One problem is apparently the very small ratio of backscattered to total scattered energy, which becomes less restrictive as windspeed, hence, surface roughness, is increased. We also observe that within 10° of grazing, considerably larger surface realizations are required to capture the extensive multiple scatter. Additional results are presented for the windspeed dependence of sea surface backscatter over a range of incidence angles. Although published measurements are relatively scarce, several qualitative characteristics of the results are in agreement with radar backscatter data.

## APPENDIX A
## GENERALIZED CONJUGATE RESIDUAL (GCR)

For the preconditioned GCR solution of (18), we first calculate

$$\begin{aligned} \mathbf{r}^0 &= \mathbf{C} - \mathbf{Z}\mathbf{X}^0 \\ \mathbf{z}^0 &= \tilde{\mathbf{Z}}^{-1}\mathbf{r}_0 \\ \mathbf{h}^0 &= \mathbf{z}^0 \end{aligned} \tag{A.1}$$

where $\mathbf{X}^0$ is the initial guess, which may be taken to be $\mathbf{X}^0 = \tilde{\mathbf{Z}}^{-1}\mathbf{C}$ or simply $\mathbf{X}^0 = \mathbf{0}$. Given (A.1), the equations

$$\begin{aligned} \mathbf{X}^{n+1} &= \mathbf{X}^n + \alpha^n \mathbf{h}^n \\ \mathbf{r}^{n+1} &= \mathbf{r}^n - \alpha^n \mathbf{Z}\mathbf{h}^n \\ \mathbf{z}^{n+1} &= \tilde{\mathbf{Z}}^{-1}\mathbf{r}^{n+1} \\ \mathbf{h}^{n+1} &= \mathbf{z}^{n+1} - \beta^n \mathbf{h}^n \end{aligned} \tag{A.2}$$

where

$$\alpha^n = \frac{(\mathbf{r}^n,\, \mathbf{Z}\mathbf{h}^n)}{(\mathbf{Z}\mathbf{h}^n, \mathbf{Z}\mathbf{h}^n)}, \quad \beta^n = \frac{(\mathbf{Z}\mathbf{z}^{n+1},\, \mathbf{Z}\mathbf{h}^n)}{(\mathbf{Z}\mathbf{h}^n,\, \mathbf{Z}\mathbf{h}^n)} \tag{A.3}$$

are iterated in $n(n = 0,\, 1,\, 2,\, \cdots)$ until the residual $\|\mathbf{r^n}\|$ meets the convergence criterion $\|\mathbf{r^n}\| < \epsilon$. For calculations in this paper, the value $\epsilon = 10^{-4}$ is used throughout. Using the $\ell_2$ norm, this criterion guarantees that the maximum error at any point in the domain is very small. Values of $\epsilon$ from $10^{-4}$–$10^{-5}$ are typically observed. The notation ( , ) in (A.3) denotes the inner product. At each iteration, the optimal parameters $\alpha$, $\beta$ can be found by minimizing the functionals $(\mathbf{r}^{n+1},\, \mathbf{r}^{n+1})$ and $(\mathbf{Z}\mathbf{h}^{n+1},\, \mathbf{Z}\mathbf{h}^{n+1})$ with respect to $\alpha$ and $\beta$, respectively.

## REFERENCES


[1] R. F. Harrington, *Field Computation by Moment Methods.* New York: Macmillan, 1968.

[2] L. Tsang, C. H. Chan, K. Pak, and H. Sangani, "Monte Carlo simulations of large-scale problems of random rough surface scattering and applications to grazing incidence with the BMIA/canonical grid method," *IEEE Trans. Antennas Propagat.,* vol. 43, pp. 851–859, Aug. 1995.

[3] K. Pak, L. Tsang, and C. H. Chan, "Backscattering enhancement of electromagnetic waves from two-dimensional perfectly conducting random rough surfaces based on Monte Carlo simulations," *J. Opt. Soc. Amer,* vol. 12, pt. A, pp. 2491–2499, 1995.

[4] L. Tsang, C. H. Chan, and H. Sangani, "Banded matrix iterative approach to Monte Carlo simulations of scattering of waves by large-scale random rough surface problems: TM case," *Electron. Lett.,* vol. 29, pp. 1153–1154, 1993.

[5] K. Pak, L. Tsang, and J. T. Johnson, "Numerical simulations and backscattering enhancement of electromagnetic waves from two-dimensional dielectric random rough surfaces with the sparse-matrix canonical grid method," *J. Opt. Soc. Amer.,* vol. 14, pt. A, pp. 1515–1529, 1997.

[6] J. T. Johnson, L. Tsang, R. T. Shin, K. Pak, C. H. Chan, A. Ishimaru, and Y. Kuga, "Backscattering enhancement of electromagnetic waves from two-dimensional perfectly conducting random rough surfaces: A comparison of Monte Carlo simulations with experimental data," *IEEE Trans. Antennas Propagat.,* vol. 44, pp. 748–756, May 1996.

[7] H.-C. Ku and B. Ramaswamy, "Multi-grid domain decomposition approach for solution of Navier–Stokes equations in primitive variable form," *Int. J. Numer. Methods Eng.,* vol. 38, pp. 667–683, 1995.

[8] H.-C. Ku, "Solution of flow in complex geometries by the pseudospectral element method," *J. Comput. Phys.,* vol. 117, pp. 215–227, 1995.

[9] A. Pao and M. Mow, *Diffraction of Elastic Waves and Dynamic Stress Concentrations.* Russak, NY: Crane, 1973.

[10] Y. Saad and M. H. Schultz, "GMRES: A generalized minimal residual algorithm for solving nonsymmetric linear systems," *SIAM J. Stat. Comput.,* vol. 7, pp. 856–869, 1986.

[11] Y. S. Wong, T. A. Zang, and M. Y. Hussaini, "Preconditioned conjugate residual methods for the solution of spectral methods," *Comput. Fluids,* vol. 14, pp. 85–89, 1986.

[12] E. I. Thorsos, "The validity of the Kirchhoff approximation for rough surface scattering using a Gaussian roughness spectrum," *J. Acoust. Soc. Amer.,* vol. 83, p. 78, 1988.

[13] A. W. Bjerkaas and F. W. Riedel, "Proposed model for the elevation spectrum of a wind-roughened sea surface," Johns Hopkins Univ. Appl. Phys. Lab., vol. TG-1328, 1979.

[14] W. Hackbush, *Multi-Grid Methods and Applications.* Berlin, Germany: Springer-Verlag, 1985.

[15] A. Brandt, "Multi-level adaptive solutions to boundary-value problems," *Math. Comput.,* vol. 31, pp. 333–390, 1977.

[16] K. Kalbasi and K. R. Demarest, "A multi-level formulation of the method of moments," *IEEE Trans. Antennas Propagat.,* vol. 41, pp. 589–598, May 1993.

[17] P. Wesseling, *An Introduction to Multigrid Methods.* London, U.K.: Wiley, 1992.

[18] S.-L. Chuang and J. A. Kong, "Scattering of waves from periodic surfaces," *Proc. IEEE,* vol. 69, pp. 1132–1144, Sept. 1981.

[19] K. A. Zaki and A. R. Neureuther, "Scattering from a perfectly conducting surface with a sinusoidal height profile: TE polarization," *IEEE Trans. Antennas Propagat.,* vol. AP-19, pp. 208–214, Mar. 1971.

[20] ———, "Scattering from a perfectly conducting surface with a sinusoidal height profile: TM polarization," *IEEE Trans. Antennas Propagat.,* vol. AP-19, pp. 747–751, Nov. 1971.

[21] J. R. Kuttler and J. D. Huffaker, "Solving the parabolic wave equation with a rough surface boundary condition," *J. Acoust. Soc. Amer.,* vol. 94, pp. 2451–2454, 1993.

[22] D. R. Thompson and R. D. Chapman, "Note on the reduction of the full-wave method for rough surface scattering to the small height limit," *J. Geophys. Res.,* vol. C3-98, pp. 4827–4831, 1993.

[23] L. C. Schroeder, P. R. Schaffner, J. L. Mitchell, and W. L. Jones, "AAFE RADSCAT 13.9-GHz measurements and analysis: Wind-speed signature of the ocean," *IEEE J. Oceanic Eng.*, vol. OE-10, pp. 346–357, Oct. 1985.
[24] H. Masuko, K. Okamoto, M. Shimada, and S. Niwa, "Measurement of microwave backscattering signatures of the ocean surface using X band and Ka band airborne scatterometers," *J. Geophys. Res.*, vol. C11-91, pp. 13065–13083, 1986.
[25] L. B. Wetzel, "Sea clutter," in *Radar Handbook*, M. Skolnik, Ed. New York: McGraw-Hill, 1990.
[26] D. R. Thompson, "Calculations of radar backscatter modulations from internal waves," *J. Geophys. Res.*, vol. C10-93, pp. 12371–12380, 1988.

**Denis J. Donohue** received the B.A. degree in computer science from Rutgers University, Piscataway, NJ, in 1985 and the Ph.D. degree in electrical engineering from Stanford University, Stanford, CA, in 1991.

Following a Postdoctoral appointment working in space plasma physics, he joined the Research and Technology Development Center of the Johns Hopkins University Applied Physics Laboratory, Laurel, MD. His research interests span a broad range including space science and astrophysics, optics, acoustics, electromagnetic theory, and computational physics. His emphasis, for several years, has been on radar and optical scattering from the ocean surface.

Dr. Donohue is a member of the IEEE Antennas and Propagation Society and the U.S. National Committee of URSI (Commission F).

**Hwar-Ching Ku** received the B.S. degree from Tsing Hua University, Hsinchu, R.O.C., in 1976, the M.S. degree from Taiwan University, Tapei, in 1980, and the Ph.D. degree from Illinois Institute of Technology, Chicago, in 1984, all in chemical engineering.

He joined the Johns Hopkins University Applied Physics Laboratory, Laurel, MD, in 1985, where he is now a Senior Staff Member in the Research and Technology Development Center. Most of his research interests in computational physics include fluid dynamics, magnetohydrodynamics of space, plasma dynamics of aerospace, and electromagnetic scattering from the ocean surface.

**Donald R. Thompson** received the B.S. degree in physics from Case Western Reserve University, Cleveland, OH, in 1964, and the Ph.D. degree in theoretical physics from the University of Minnesota, Minneapolis, MN, in 1968.

Early in his career, he studied problems in few-body nuclear reactions and stellar nucleosynthesis at the California Institute of Technology, Pasadena, the University of Minnesota, and the Universität Tübingen, Tübingen, Germany. Since joining the Johns Hopkins University Applied Physics Laboratory, Laurel, MD, in 1980, his research has focused on the physics of ocean surface waves and electromagnetic scattering from the ocean surface.